3D Reconstruction of Sawtooth 180° Tail-to-Tail Domain Walls in Single Crystal $BiFeO_3$

Wanbing Ge[(1)*], Richard Beanland[(1)], Marin Alexe[(1)] and Ana M. Sanchez[(1)*]

Wanbing Ge, Richard Beanland, Marin Alexe and Ana M. Sanchez
Department of Physics, University of Warwick, Coventry CV4 7AL, United Kingdom
E-mail: Wanbing.Ge@warwick.ac.uk, A.M.Sanchez@warwick.ac.uk

Keywords: Bismuth ferrite, ferroelectric domains, 180° domain walls, sawtooth domain walls

Previous studies of single crystal $BiFeO_3$ have found a dense domain structure with alternating sawtooth and flat domain walls (DWs). The nature of these domains and their three-dimensional structure has remained elusive to date. Here, we use several sections taken at different orientations to examine the structure in detail, concentrating here on the sawtooth DWs using diffraction contrast transmission electron microscopy, electron diffraction, and aberration-corrected scanning transmission electron microscopy (STEM). All DWs are found to be 180-degree type; the flat walls have head-to-head polarity while the sawtooth DWs are tail-to-tail with peaks elongated along the polar [111] axis, formed by neutral $(11\bar{2})$ DW facets and slightly charged facets with orientations close to $(3\bar{2}1)$ and $(\bar{3}21)$. The neutral DW facets are Ising type and very abrupt, while the charged DW facets have mixed Néel/Bloch/Ising character with a chiral nature and a width of approx. 2 nm.

1. Introduction

Domains form in ferroic materials to minimize the total system energy, consisting of electrostatic, magnetic, and elastic components[1]. At the boundaries between them, regions known as domain walls (DWs), the material has a locally varying structure where the order parameter that characterises functionality, (e.g. in ferroelectrics the spontaneous polarization $\mathbf{P}_s$), adapts its orientation and/or magnitude over a finite distance. The configurations of ferroelectric domain walls have attracted much attention for the interesting physics they reveal.[2–5] Here, we examine domains in single-crystal $BiFeO_3$, one of the most widely studied functional materials, which exhibits simultaneous ferroelectric, antiferromagnetic and ferroelastic order at room temperature.[6] These $BiFeO_3$ crystals have been shown to contain a dense three-dimensional network of domain walls [7–9] that presents several challenges in

characterisation and interpretation. Understanding their structure and formation is important for future domain wall applications, in which they may be manipulated, written, erased, and moved to play an active role in future electronic devices.[1,10]

Bulk $BiFeO_3$ has a rhombohedral structure (space group*R3c*, No. 161) below its Curie temperature T_c = 1100K with lattice parameter of 3.965 Å and rhombohedral angle 89.4°, sufficiently close to 90° for it to be considered pseudocubic (pc indexing is used throughout this work). Oxygen octahedra in each neighbouring unit cell are tilted by ~14° antiphase about the three-fold [111] axis ($a^-a^-a^-$ in Glazer notation[11]). Its spontaneous ferroelectric polarization $\mathbf{P}_s$ = 100 μC cm^{-2} along <111> arises mostly from the displacement of the Bi ions relative to their surrounding FeO_6 cages.[12] Domain walls are classified according to the angle between the different directions of $\mathbf{P}_s$ on each side, giving three types: 71°, 109° and 180°.[13,14]

The batch of flux-grown single-crystals of $BiFeO_3$ investigated here have been subject to several previous investigations,[7,8,15] all of which have revealed a dense array of parallel domain walls seen in piezoresponse force microscopy (PFM) and conventional transmission electron microscopy (TEM) as alternating sawtooth and flat bands of contrast. The complex microdomain structure in these crystals is extremely stable, exhibiting no change upon observation even in the thinnest specimens. The first structural study[7] showed the domain walls to be either 180°- or 109°-type, and due to the high predicted energy of 180°-type DWs it was proposed that they were probably 109°-type. A second study [8] of the same batch of crystals using negative C_s high resolution TEM imaging found a variety of DW types including 71°, 109° and 180°. The most recent study[9] confirmed the sawtooth DWs to be 180°-type and showed that they could be moved with an applied electric field, but proposed that flat DWs were 109°-type. In this article we revisit the domain structure in this same batch of crystals using a combination of PFM, conventional TEM, convergent beam electron diffraction (CBED) and atomic resolution scanning TEM (STEM). We find that there are only two domains in the crystal and all DWs are 180°-type. The difficulties experienced in previous work may be explained due to projection effects when the three-dimensional domain structure is observed in an electron transparent foil, which we overcome here by using focused ion beam (FIB) to prepare multiple sections with different orientations from the same region of crystal. Here we concentrate on the observation and analysis of sawtooth domain walls, while the structure of flat walls is explored elsewhere.[16]

2. Experimental

$BiFeO_3$ single crystals were obtained from the same batch used in the studies of Marti et al.,[15] Berger et al.,[7] and Jia et al.,[8] the latter describing growth conditions in detail. In brief, crystals were grown from $BiFeO_3$ reacted powder in a Bi_2O_3/B_2O_3 flux, cooled very slowly from 1170 K to 875 K. Much of the growth took place below the paraelectric-ferroelectric phase transition at 1098 K. Only crystals grown in the top of the melt, without any contact with the Pt crucible, were harvested for further investigation. These were octagonal shaped (001) oriented crystals with sizes of half to a few millimetres, with a top surface of four (*hhl*) facets only a few degrees away from (001). Several well-formed single crystals were selected for this study.

For PFM a crystal was ground and polished to (001) using diamond lapping film of decreasing sizes to 0.1 µm, finishing with a dilute 0.04 µm colloidal silica solution. PFM measurements were conducted on a Bruker Dimension Icon AFM with a drive frequency around the resonance peak and a drive voltage of 2 V.

To obtain a 3-dimentional view of the domains TEM specimens were prepared by lift-out on a Tescan Amber Ga^+ FIB-SEM from a second crystal from the same batch in its as-grown state, with (110), (010) and $(\bar{1}10)$ orientations. Cutting and thinning was performed using an ion beam energy of 30 kV, with a final low energy polish of 2 kV. The specimens were taken from a compact region on the crystal, and their orientations were verified by their relative position, selected area electron diffraction (SAED) pattern as well as atomic resolution images. To obtain the thinnest possible TEM specimen for very high-resolution imaging, wedge-shaped lamellae were produced. STEM images were taken with a double-corrected JEOL ARM 200F STEM operating at 200 kV and beam convergence semi-angle of 21 mrad. The annular bright field (ABF) and annular dark field (ADF) detectors covered 11.5-24 and ~70-280 mrad, respectively.[5] Conventional TEM images and selected area/CBED patterns were taken with a JEOL 2100 LaB_6 TEM operating at 200 kV. Atom positions in atomic resolution STEM images are located by fitting two-dimensional Gaussian peaks.[5,17]

3. Results

3.1 Domain type

Intriguingly, the domains in these $BiFeO_3$ single crystals always appear with alternating flat DWs and zig-zag sawtooth DWs, irrespective of the plane of section, or which area is chosen. The three-dimensional nature of the domains means that it is essential to obtain views from several different directions to fully understand the structure. Four different views are shown in **Figure 1**, PFM on a polished (001) face and images from three TEM lamellae cut from this

(001) surface, i.e. examined with the electron beam along [110], [010] and [$\bar{1}$10]. The different observations are brought together in the schematic of Figure 1(a) showing that the domains lie parallel to (112) on the micrometre scale.

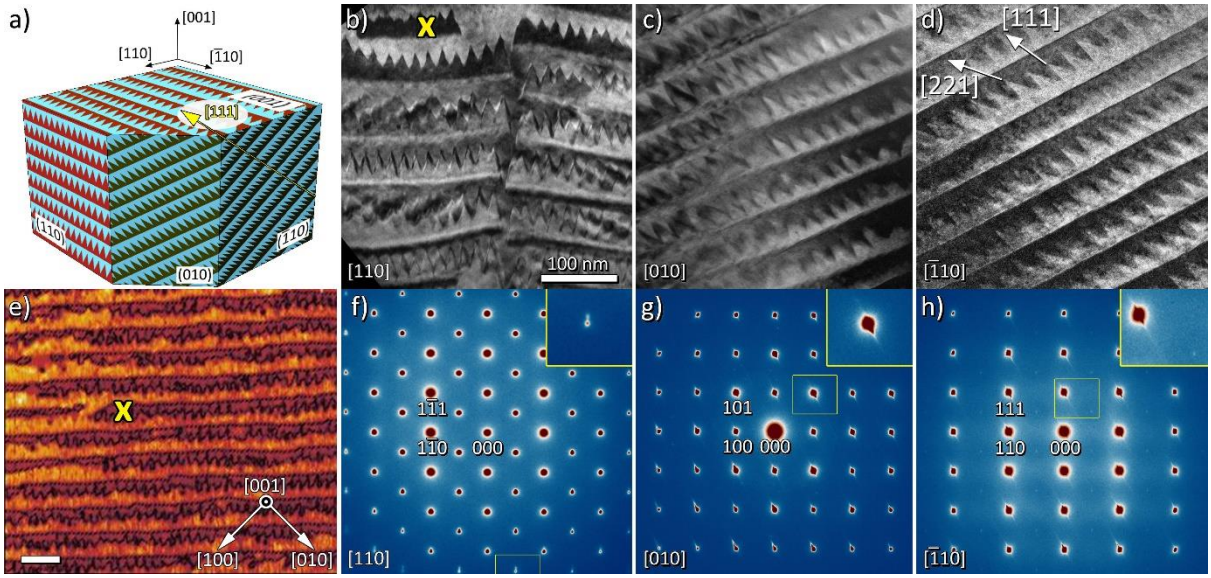

Figure 1. Domain structure in a $BiFeO_3$ single crystal. (a) Schematic showing the alternating straight and sawtooth domain walls as seen on different sections through the crystal. (b-d) diffraction contrast TEM images taken in [110], [010] and [$\bar{1}$10] sections, respectively. The 100nm scale bar applies to all three micrographs. e) PFM out-of-plane amplitude image of a (001) polished surface (scan direction vertical in this image), scale bar 100 nm; (f-h) selected area diffraction patterns corresponding to (b-d). Closed domains, showing that sawtooth and flat domain walls are of the same type but opposite polarity, are marked in (b) and (e) by a yellow **x**. Insets in the diffraction patterns show reciprocal lattice streaking, caused by the flat (112) domain walls.

We first consider the crystal polarity and the type of domain wall. It is apparent from regions where the periodicity of the domain structure is interrupted that a sawtooth DW can curve round and become a flat DW, completely enclosing a domain (e.g. that marked in Figs. 1b and 1e by x). This observation suggests that the sawtooth and flat DWs therefore simply have opposite polarities. We now consider the PFM and selected area electron diffraction pattern (SADPs) of Figure1 to deduce the relationship between them.

PFM observations agree with those of Berger,[7] showing a change in the phase of the PFM signal across the domain walls for both out-of-plane (OOP) and in-plane (IP) components (supplementary **Figure S1**). All the eight different polarities in an *R3c* perovskite are shown in **Figure 2**(a)-(h), both as cubes and (001) stereographic projections with the [111] polar

axis marked ⊕. The phase reversal of the out-of-plane (OOP) PFM component indicates that one domain must be found in the top row (a), (b), (c), (d) and the other in the bottom row (e), (f), (g), (h) of Figure 2. The in-plane (IP) component of polarisation in a PFM scan is detected by torsion of the cantilever and is thus sensitive only to the component parallel to the scan. With a [110] scan direction a strong IP signal, as observed in our measurements, is only found for the orientations in Figure 2(a), (d), (e) and (h), eliminating the other possibilities. Simultaneous reversal of both IP and OOP signals indicates a 180° reversal of polarity, with domain orientations Figure 2(a)+(h) or (d)+(e), but it is not possible between these two options from PFM alone.

Complementary information can be provided by SADPs at <110> zone axes, which have half odd-odd-odd (½ *ooo*) spots only when the zone axis is not perpendicular to the [111] polar axis.[18,19] These zone axes are marked in red (with ½ *ooo*) and blue (without ½ *ooo*) on Figure 2. With a selected area aperture of several hundred nm in diameter, the diffraction patterns sample many domains and the lack of ½ *ooo* spots in the $[\bar{1}10]$ SADP, Figure 1(h), therefore indicates that the polar axis is perpendicular to the electron beam in both domains. The SADPs of Figs. 1(f) and (h) are marked in Figure 2 by A and B respectively and the condition that B must remain blue for both domains once again limits the possible domain orientations to (a), (d), (e) and (h). Furthermore, the small deviation from cubic symmetry results in splitting of spots in SAED patterns across 70.5° and 109.5° domain walls in $BiFeO_3$.[18] The lack of any such splitting thus indicates that the domain walls are of 180° type. From SADP we are therefore sure that the domain walls must be of 180° type, with the same two possibilities as given by PFM, i.e. Figure 2(a)+(h) or (d)+(e), but again cannot uniquely distinguish the polar axis. To obtain a definitive answer, a technique that is sensitive to absolute structure is required that can be applied to individual domains. Since Friedel's law is not obeyed by dynamical electron diffraction,[20] the intensities of ±g diffracted beams are different in polar structures, allowing the absolute orientation of the crystal to be determined. However since the SAED patterns average across several domains, this information is superposed and cannot be seen.

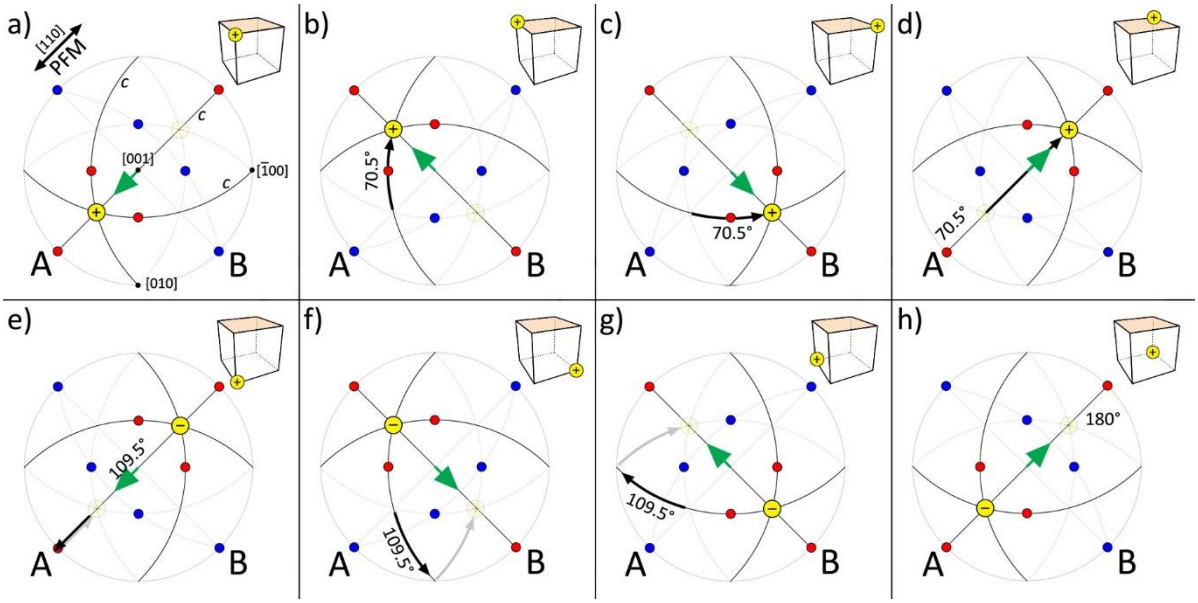

Figure 2. The eight possible orientations of the [111] polar axis in *R3c* $BiFeO_3$ shown on cubes (with shaded (001) face) and on {001} stereographic projections as yellow circles with polarity + or -. The traces of the three *c*-glide planes are marked by solid lines, all other traces shown in grey. <110> diffraction patterns with ½*ooo* spots are shown as red dots, and those without are shown in blue. The polar axis on the opposite side of the projection is shown as a faint yellow circle and the in-plane component of the polarisation is shown by the green arrow. The [110] PFM scan direction is shown in (a), and the SAED patterns of Figs. 1(f) and (h) are marked as A and B.

In CBED the electron probe can be made small enough (<10 nm diameter) to be placed inside individual domains, avoiding the averaging effect of SAED. The patterns obtained from such a measurement at the [110] zone axis are shown in **Figure 3**(a)-(d). The CBED patterns from both domains have ½ *ooo* spots and ($\bar{1}$10) mirror symmetry, with intensities in Figure 3b and 3c that are related by a 180° rotation or horizontal (001) mirror plane. Figure 3(d) shows a simulated pattern at a specimen thickness of 10.6 nm with a known direction of polarization. Comparing simulation with experiment reveals that polarization points towards flat DWs and away from sawtooth DWs. A similar set of [$\bar{1}$10] CBED measurements is shown in Figure 3(e)-(h). The patterns of Figs. 3(f) and 3(g) have no mirror symmetry, and here the intensities in adjacent domains are related by a 180° rotation. Comparison with simulation, Figure 3(h), gives the direction of polarization. These results are consistent with the [110] CBED measurement, showing the flat walls have head-to-head polarisation and the sawtooth walls have tail-to-tail polarisation. They are also consistent with the PFM and SAED observations

and with consideration to Figure 2 these results eliminate (d) and (e), showing that the two domains present are those shown in Figs. 2(a) and (h).

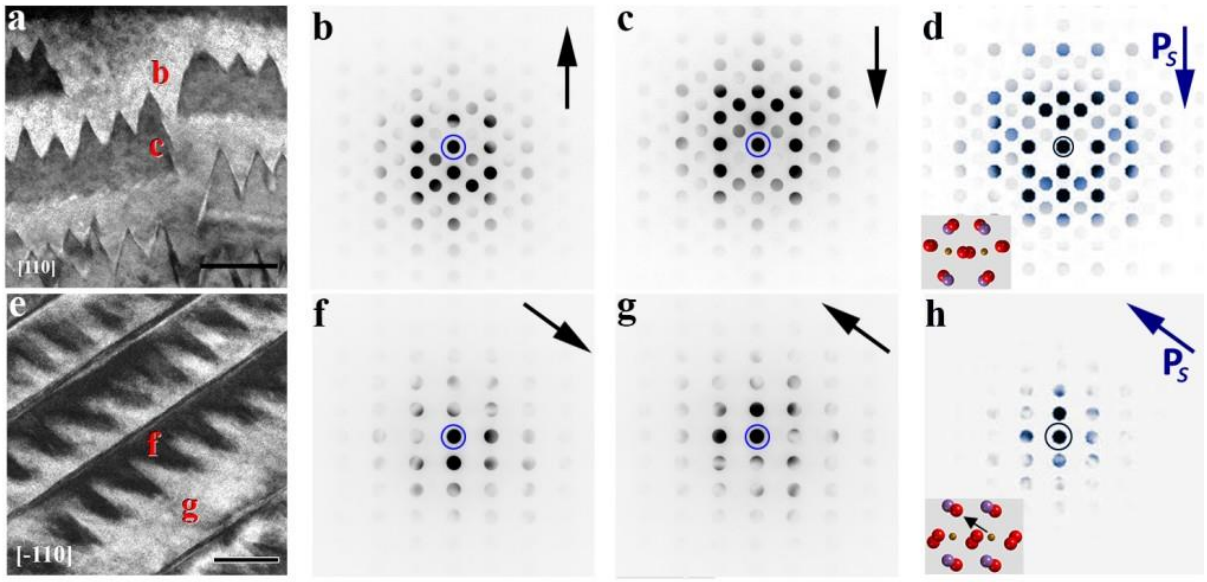

Figure 3. CBED measurements at the [110] zone axis (a-d) and the [$\bar{1}$10] zone axis (e-h). (a, e) Dark field **g** = 001 diffraction contrast TEM images (scale bar 50 nm) showing the locations used for CBED patterns. (d, h) Multislice simulations of CBED patterns at specimen thicknesses of 10.6 nm and 81.6 nm, respectively. Insets show the corresponding unit cell projection, and the direction of polarisation is marked $\mathbf{P}_s$. The **g** = 000 direct beam is circled in all patterns as an aid to the eye.

3.2 Domain geometry

Having established the type of domain wall, we now consider the domain structure. The flat walls are seen edge-on in the [$\bar{1}$10] TEM image of Figure 1d and lie on the (112) plane, 70.5° to the [111] polar axis, with a spacing of 50-100 nm. They produce streaks along [112] in the [$\bar{1}$10] selected area diffraction pattern (SADP), shown in the inset for Figure 1h. In other orientations, these streaks have the direction of [112] projected onto the diffraction plane. Thus, in the [010] SADP, streaks are seen along [102] (inset, Figure1g), while in the [110] SADP the streak is strongly inclined to the Ewald sphere, producing a subsidiary spot visible on reflections far away from the direct beam aligned with [001] (inset, Figure1f). As described in the partner article,[16] these flat head-to-head walls form around a negatively-charged Fe-rich, Bi- poor monolayer that is formed on the (112) plane during crystal growth. The tail-to-tail sawtooth DW is difficult to characterise due to its three-dimensional nature and varying appearance when seen from different viewpoints. Its straight DW segments show

that it is faceted, although in most projections the facets are seen obliquely and DWs are not edge-on. In the thinnest part of the (110) TEM specimen (top, Figure 1(b) and Figure 3(a)) the DW has a W shape, with peaks that have a spacing of 30-40 nm and symmetrical vertices (consistent with the mirror symmetry of the diffraction pattern). However, in thicker parts of the same sample multiple peaks are seen in projection, and peaks appear in arrays that are aligned in some direction offset to the point of view (bottom Figure 1(b)). In the $(\bar{1}10)$ TEM specimen, the structure is asymmetric, with the peaks pointing towards the polar direction. Since the average orientation of the tail-to-tail DW is dictated by the adjacent (112) flat head-to-head walls it must be, on average, a charged domain wall (CDW). However, as can be observed in Figure 1(d) and supplementary **Figure S2**, re-entrant $(11\bar{2})$ facets are clearly visible edge-on in the $(\bar{1}10)$ section and since this plane contains the [111] polar axis, these are neutral domain wall facets (NDWs). Based on the stereology of these TEM observations we propose that the tail-to-tail DWs form a crinkled 3D structure shown schematically in **Figure 4**, comprised of three-faceted peaks consisting of a $(11\bar{2})$ NDW and two CDWs with orientations close to $(3\bar{2}1)$ and $(\bar{3}21)$.

While the energy of any given DW configuration requires the calculation of short- and long-range electrostatic and polarisation/screening components for all DW facets and surrounding material,[21,22] it is not immediately obvious that a crinkled DW that has re-entrant facets (and thus a larger CDW area than a flat DW) is the lowest energy configuration. The presence of these facets therefore requires some consideration. Importantly, the 180° ferroelectric DWs are inherently more flexible than 71° or 109° ferroelectric-ferroelastic DWs, since the latter have two constraints, i.e. matching of lattice planes to minimise strain[23] and continuity of oxygen octahedral rotations across the DW.[24,25] These constraints favour certain orientations and control the geometry of ferroelastic DW configurations. Conversely, both octahedral rotations and lattice strain are unaffected in principle by a change in polarisation magnitude (including reversal), allowing 180° DWs to take any orientation. The formation of re-entrant facets from an initially flat tail-to-tail (112) CDW may be understood using the principle that the local energy per unit area of a DW increases with its charge density, proportional to $\mathbf{P}_s \cdot \mathbf{n}$, where $\mathbf{n}$ is the unit normal. Thus, NDWs have very low energy per unit area, and CDWs have an energy per unit area that increases as $\mathbf{n}$ is more parallel to $\mathbf{P}_s$, i.e. the [111] polar axis. A flat CDW is unstable if the local reduction in energy, produced by a change in CDW orientation that gives lower $\mathbf{P}_s \cdot \mathbf{n}$, is larger than the increase in energy arising from the increased DW area (that must take place, if the average orientation of the DW remains unchanged). To understand how the crinkled surface develops, it is instructive to first

consider a corrugated surface consisting of just two facets as shown in Figure 4a. Due to the angle between $\mathbf{P}_s$ and the DW, an 'up' step *A* rotates the local DW normal away from $\mathbf{P}_s$ while a 'down' step *Z* does the opposite. Therefore, energy is lowered at the *A* step and there is a driving force for it to expand into a re-entrant NDW facet *A*'*A*". Conversely, local energy is increased at the *Z* step, which suppresses the formation of non-re-entrant NDW facets. This means that re-entrant facets readily form to reduce local energy - even though a lower total CDW wall area, and perhaps lower total energy, could be achieved with facets that form a surface that is not re-entrant.

In three dimensions, further reduction of local energy can be obtained by CDW orientations that further minimise $\mathbf{P}_s \cdot \mathbf{n}$, i.e. forming peaks rather than corrugations. Such a structure can be obtained from an initial flat CDW by an array of nodes of alternating type, labelled *A* and *B* (Figure 4b). The nodes *A* act as nucleation sites for NDWs that expand to form diamond-shaped re-entrant NDW facets with vertices *A'*, *B*, *A*" and *B* as shown in Figure 4b. The 3D shape is illustrated in Figure 4c where it can be seen that *A'* vertices move downwards while *A*" vertices move up. Although the real structure appears much less regular than the illustration of Figure 4, this model satisfies the requirement that the domain wall must be continuous and agrees with all the observations of Figure 1 (and indeed all other investigations of these crystals[7,8]).

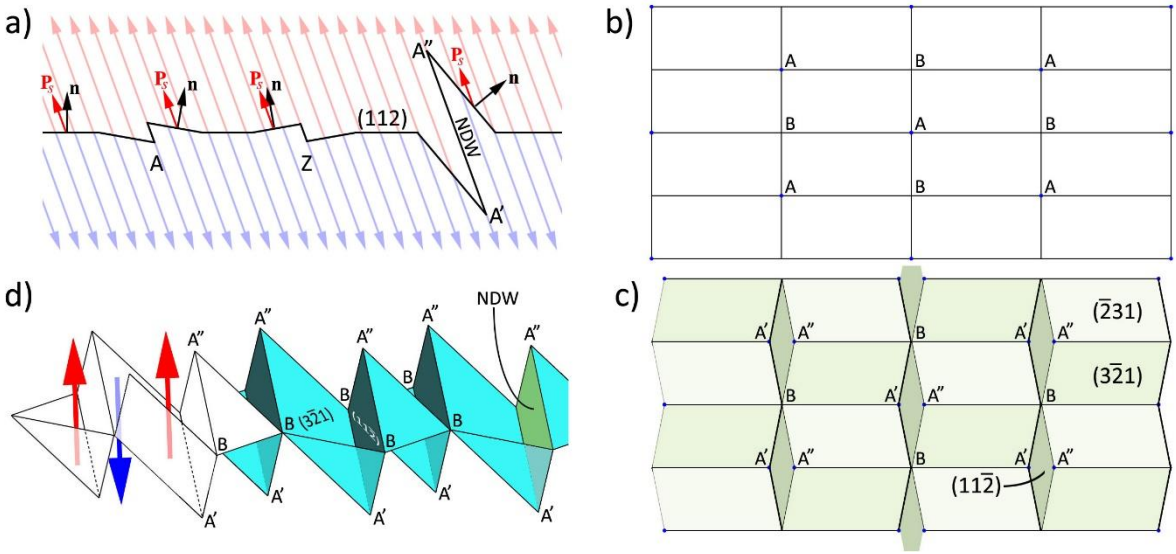

Figure 4. Formation and geometry of the crinkled tail-to-tail DW. (a) side view of a flat (112) DW, which lies at 70.5° to the polar vector $\mathbf{P}_s$. An 'up' step *A* (left) produces a local change in orientation decreasing $\mathbf{P}_s \cdot \mathbf{n}$, while a 'down' step *Z* (right) gives a local increase in $\mathbf{P}_s \cdot \mathbf{n}$ and DW energy. Growth of the step *A* into a NDW facet *A*'*A*" results in a re-entrant

sawtooth corrugated structure. (b, c) In three dimensions, an array of nodes of instability *A* on the flat DW (seen from above) can develop into a crinkled structure by splitting into vertices *A*' and *A*" that bound diamond-shaped re-entrant NDWs. A complementary array of points *B* lies at junctions between facets. (d) perspective view of the crinkled DW.

3.3 Domain wall structure

Most atomic resolution studies of DW structure in $BiFeO_3$ have been performed using thin films,[26–33] which displays a variety of domain structures and DWs that are very dependent on the substrate material, the misfit strain it induces in the $BiFeO_3$ layer and the deposition methods and conditions. In these studies 180° DWs are relatively rare, and when they are present, they are constrained by the film geometry and the other DWs with which they interact. The large area of 180° DW in the single crystals examined here, and their ability to take on complex shapes, is therefore very unusual and provides a unique opportunity for their investigation. An atomic resolution study of the sawtooth DW structure in these crystals in response to applied fields has recently been presented by Condurache et al.,[9] showing that the sidewalls could be moved in response to an applied electric field while the peaks remained pinned and immobile. The flat DWs remained pinned by the charged defects at their centre. Their use of <100> sections, in which DWs do not naturally appear edge-on in this crinkled structure, meant that their width and atomic structure was not readily determined.

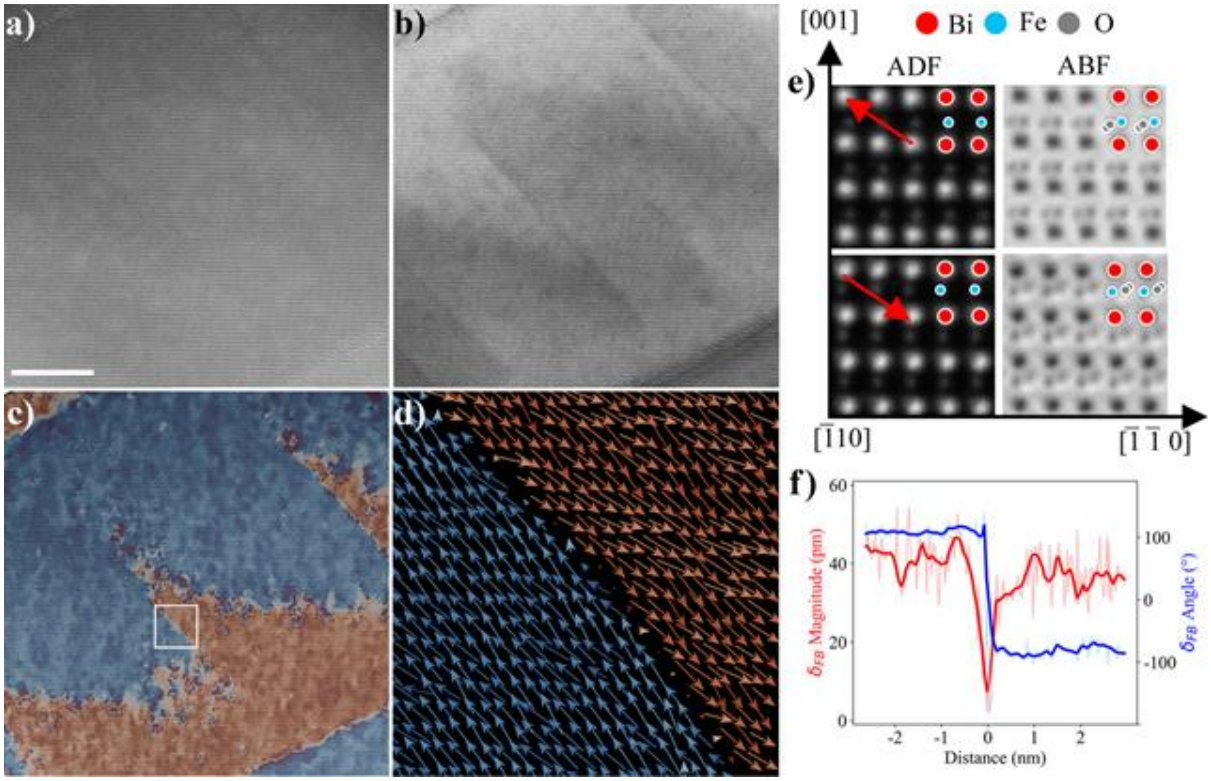

Figure 5. $\mathbf{P}_s$ map of a sawtooth 180° DW in a $(\bar{1}10)$ section. (a, b) Simultaneously collected atomic resolution ADF and ABF STEM images, scale bar 10 nm. (c) Map of the magnitude of $-\boldsymbol{\delta}_{FB}$, extracted from (a). (d) $-\boldsymbol{\delta}_{FB}$ quiver map for the boxed region in (c), where the NDW facet is captured cleanly. (e) Higher magnification ADF and ABF STEM images from the two domains showing the measurement of $\boldsymbol{\delta}_{FB}$ and the crystal orientation. (f) Magnitude and angle of $-\boldsymbol{\delta}_{FB}$ across the boundary in (d).

Here, with the use of different sections, we may view DWs without projection effects, in particular in the $(\bar{1}10)$ orientation the $(11\bar{2})$ NDW facets can be captured cleanly. An example is shown in the atomic resolution images of **Figure 5**. In the BF-STEM image Figure 5(b), the $(3\bar{2}1)$ and $(\bar{3}21)$ CDW facets are almost parallel to the plane of section, perpendicular to the electron beam, and appear as diffuse darker bands. The$(11\bar{2})$ NDW facets are seen exactly edge-on and appear as sharp dark lines along [111]. On a unit-cell level, polarisation $\mathbf{P}_s$ is commonly taken to be proportional to the negative of the displacement of the Fe atom column relative to its surrounding Bi atom columns, namely $-\boldsymbol{\delta}_{FB}$.[34–37] As illustrated in Figure 5(e), in the $(\bar{1}10)$ projection this displacement is relative to the mid-point of the line joining Bi atom columns along [001], and because the [111] polar axis lies in the image plane the full shift is observed. Figure 5(c) shows a map of $-\boldsymbol{\delta}_{FB}$ magnitudes obtained from on the ADF-STEM image of Figure 5(a) using two-dimensional Gaussian fitting.[5,17] The result confirms that $-\boldsymbol{\delta}_{FB}$ reverses direction across the DW and has roughly the same magnitude of ~40 pm in the two domains, in good accordance with the theoretical value of 41 pm. The correlation between the CDW bands in Figures 5(b) and (c) is quite poor; while they appear very diffuse in the ABF image, they present as sharp, but irregular, DWs in the $\boldsymbol{\delta}_{FB}$ map. Condurache et al.[9] found that the BF-STEM contrast of these DWs did not follow their movement under an applied field, and suggested that the contrast was due to a concentration of oxygen vacancies that had accumulated at the original position of the DW. This may also be the case here, although it is certain that the DW is seen in projection through the thickness of the TEM specimen, with varying polarisation along the electron beam. The apparent sharp location of the DW may be due to the reduced depth of field in atomic resolution STEM images,[38] in which case it would be very sensitive to imaging conditions such as defocus. For these reasons, the $-\boldsymbol{\delta}_{FB}$ measurements cannot be taken as reliable at the CDWs in this projection, nor give useful information about the local polarisation at the CDW. In comparison, the $(11\bar{2})$ NDW appears sharp and straight in Figure 5(c) and is concurrent with the dark line in Figure 5(b), giving confidence that $-\boldsymbol{\delta}_{FB}$ measurements have meaning. Figure

5(d) shows a quiver plot, and 5(f) a line plot, of $-\boldsymbol{\delta}_{FB}$ for the NDW highlighted in Figure 5(c). No rotation of polarisation is apparent at the DW; rather, $-\boldsymbol{\delta}_{FB}$ drops to zero for a single unit cell at the DW. This neutral domain wall is thus of Ising type. The magnitude of polarisation is also maintained up to the DW. This agrees both with predictions that NDWs are in general much sharper than CDWs,[13,39,40] and contrasts with observations of other CDWs in $BiFeO_3$ including 180° DWs[2,31,41] and 71°/109° DWs [31,35,42,43] as well as the tail-to-tail CDW facets described below.

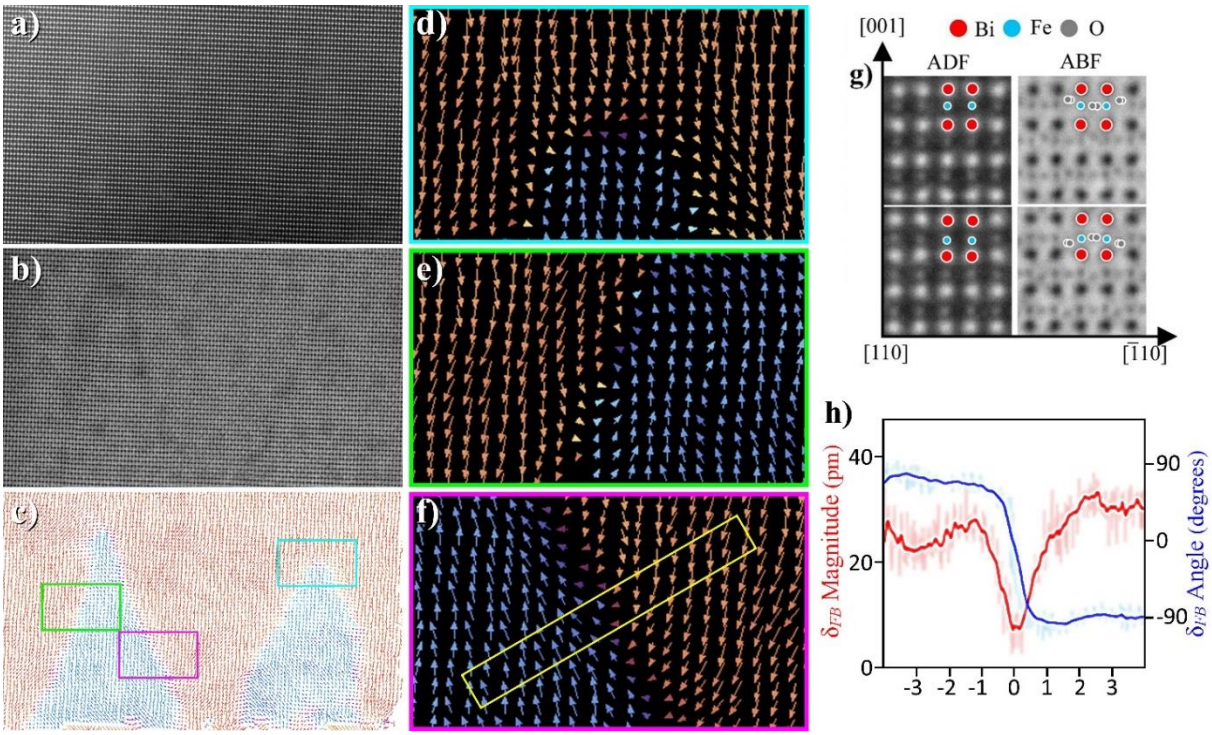

Figure 6. $\mathbf{P}_s$ map of a sawtooth 180° DW in a (110) section. (a-c) Simultaneously collected atomic resolution STEM DF and BF images, and the corresponding $-\boldsymbol{\delta}_{FB}$ vector quiver map. Scale bar is 5 nm. (d-f) Enlarged version of the boxed regions in (c). (g) Atomic resolution STEM ADF and ABF images showing $BiFeO_3$ unit cells in the two domains. (h) Magnitude and angle of $-\boldsymbol{\delta}_{FB}$ along the boxed region in (f).

The orientation of the CDW facets means that no low-index zone axis is available that would allow them to be imaged at atomic resolution and edge-on. However, they are inclined by only ~10° from the point of view in a (110) section, and by choosing the very thinnest part of the specimen we may hope to minimise projection effects and obtain a reliable measurement of $-\boldsymbol{\delta}_{FB}$ at the unit cell level, as shown in **Figure 6**. Here, the tips of two peaks are shown, corresponding to vertices of type *A*' in Figure 4, bounded by CDWs. In this projection, the $(11\bar{2})$ NDW facets lie at ~20° to the plane of section. If one of these facets is captured in the TEM lamella, there will be a 180° change of polarisation at some point in the specimen,

leading to unreliable results as observed for the CDWs in the $(1\bar{1}0)$ section. However, with a distance between NDW facets of ~40nm and an estimated specimen thickness of ~7nm it is unlikely that one has been captured in the region of Figure 6, meaning that the polarisation should not change significantly through its thickness. Confidence in the results is bolstered by the coincidence between the DW location in the ABF image Figure 6(b) and $-\boldsymbol{\delta}_{FB}$ map Figure 6(c). The average value of δ_{FB} measured away from the DW is 23 pm, as expected for this (110) projection – the component of 34 pm parallel to the electron beam is not observed – and antiphase tilting of oxygen octahedra is clearly visible as a curvature of O-Fe-O-Fe-O chains in the ABF images (Figure 6g). Figures 6(d), (e) and (f) show enlarged parts of the quiver plot at the tip of the domain and on the sidewalls, respectively. At the tip of the domain where the DW is perpendicular to the polar axis, Figure 6(d), there is no obvious trend in the orientation of $\mathbf{P}_s$ and its magnitude drops close to zero, i.e. the DW has Ising character. Figure 6(f) shows a region away from the tip where the 180° change in $\mathbf{P}_s$ is uniform and the DW is flat, with a plot of the orientation and magnitude of $\mathbf{P}_s$ in the marked region given in Figure 6(h). Here, $\mathbf{P}_s$ rotates clockwise as the DW is crossed from right ($\mathbf{P}_s$ down) to left ($\mathbf{P}_s$ up) and in contrast to the very abrupt change in $\mathbf{P}_s$ seen at the NDW facet in Figure 5, this Néel-type rotation occurs over a width of almost 2nm. There is also a decrease in the magnitude of $\boldsymbol{P}_s$, over the same width, dropping almost to zero at the DW centre. Even though the $\mathbf{P}_s$ component parallel to the point of view is not seen, this reduction indicates that the DW also has Ising- and/or Bloch-type character, with a reduced magnitude and/or rotation of $\mathbf{P}_s$ to lie along [110]. This is perhaps to be expected since the mixed Néel/Bloch/Ising-type of CDWs in ferroic materials is well established,[44] and both 71° and 109° CDWs in thin-film $BiFeO_3$ have been confirmed to have a chiral nature.[45,46] Interestingly, the clockwise rotation of $\mathbf{P}_s$ seen in Figure 6(f) is not found in all places along the sawtooth DW, and regions can also be found with anticlockwise rotation. Between the two chiralities, an interfacial line defect forms with vortex or skyrmionic character as shown in Figure 6(e).

4. Summary and Conclusion

We have re-examined the domain structure in $BiFeO_3$single crystals, using TEM imaging, electron diffraction and atomic resolution STEM in FIB-prepared sections taken in several orientations. They have a dense 180° domain structure that is dictated by the formation of charged non-stoichiometric monolayers on (112) planes, which form flat, immobile head-to-head 180° CDWs with a spacing of ~100 nm, characterised in detail elsewhere.[16] Between them, tail-to-tail 180° walls form a crinkled, sawtooth DW with peaks elongated along the

[111] polar axis, bounded by facets with orientations close to $(3\bar{2}1)$, $(\bar{3}21)$ and $(11\bar{2})$. Their formation is driven by the reduction in the local charge per unit area for DW facets that maximise the angle between their normal **n** and the polar axis $\mathbf{P}_s$. The 70° angle between $\mathbf{P}_s$ and the average (112) plane of the DW favours the formation of re-entrant $(11\bar{2})$ NDW facets, even though this results in a larger total CDW area. These NDWs are found to be Ising-type and very abrupt, with an unpolarised centre only a single unit cell in width. The CDW facets are chiral, mixed Néel/Bloch/Ising-type with a width of approx. 2 nm. These observations show the complexity that 180° domain structures can attain in three dimensions and highlights the competing driving forces that drive their formation.

Supporting Information

Supporting Information is available from the Wiley Online Library or from the author.

Acknowledgements

WG acknowledges support from EPSRC International Doctoral Scholars grant under grant number EP/R513374/1

Received: ((will be filled in by the editorial staff))
Revised: ((will be filled in by the editorial staff))
Published online: ((will be filled in by the editorial staff))

References

[1] G. Catalan, J. Seidel, R. Ramesh, J. F. Scott, *Rev Mod Phys* **2012**, *84*, 119.
[2] C. L. Jia, M. Lentzen, K. Urban, *Science (1979)* **2003**, *299*, 870.
[3] A. K. Yadav, C. T. Nelson, S. L. Hsu, Z. Hong, J. D. Clarkson, C. M. Schlepuëtz, A. R. Damodaran, P. Shafer, E. Arenholz, L. R. Dedon, D. Chen, A. Vishwanath, A. M. Minor, L. Q. Chen, J. F. Scott, L. W. Martin, R. Ramesh, *Nature* **2016**, *530*, 198.
[4] D. Rusu, J. J. P. Peters, T. P. A. Hase, J. A. Gott, G. A. A. Nisbet, J. Strempfer, D. Haskel, S. D. Seddon, R. Beanland, A. M. Sanchez, M. Alexe, *Nature* **2022**, *602*, 240.
[5] J. J. P. Peters, G. Apachitei, R. Beanland, M. Alexe, A. M. Sanchez, *Nat Commun* **2016**, *7*, DOI 10.1038/ncomms13484.
[6] G. Catalan, J. F. Scott, *Advanced Materials* **2009**, *21*, 2463.
[7] A. Berger, D. Hesse, A. Hähnel, M. Arredondo, M. Alexe, *Phys Rev B Condens Matter Mater Phys* **2012**, *85*, DOI 10.1103/PhysRevB.85.064104.
[8] C. L. Jia, L. Jin, D. Wang, S. B. Mi, M. Alexe, D. Hesse, H. Reichlova, X. Marti, L. Bellaiche, K. W. Urban, *Acta Mater* **2015**, *82*, 356.
[9] O. Condurache, G. Draž Ić,Ić, T. Rojac, H. Urš, B. Dkhil, A. Bradeš Ko, D. Damjanovic, A. Benč, *Nano Lett* **2022**, DOI 10.1021/ACS.NANOLETT.2C02857.

[10] J. Seidel, L. W. Martin, Q. He, Q. Zhan, Y. H. Chu, A. Rother, M. E. Hawkridge, P. Maksymovych, P. Yu, M. Gajek, N. Balke, S. v. Kalinin, S. Gemming, F. Wang, G. Catalan, J. F. Scott, N. A. Spaldin, J. Orenstein, R. Ramesh, *Nat Mater* **2009**, *8*, 229.
[11] A. M. Glazer, *Acta Crystallogr B* **1972**, *28*, 3384.
[12] F. Kubel, H. Schmid, *Acta Crystallographica Section B* **1990**, *46*, 698.
[13] G. Catalan, J. Seidel, R. Ramesh, J. F. Scott, *Rev Mod Phys* **2012**, *84*, 119.
[14] G. Catalan, J. F. Scott, *Advanced Materials* **2009**, *21*, 2463.
[15] X. Martí, P. Ferrer, J. Herrero-Albillos, J. Narvaez, V. Holy, N. Barrett, M. Alexe, G. Catalan, *Phys Rev Lett* **2011**, *106*, DOI 10.1103/PhysRevLett.106.236101.
[16] W. Ge, R. Beanland, M. Alexe, Q. Ramasse, A. M. Sanchez, **2023**.
[17] J. J. P. Peters, N. C. Bristowe, D. Rusu, G. Apachitei, R. Beanland, M. Alexe, A. M. Sanchez, *ACS Appl Mater Interfaces* **2020**, *12*, 10657.
[18] D. I. Woodward, I. M. Reaney, *Acta Crystallogr B* **2005**, *61*, 387.
[19] R. Beanland, P. A. Thomas, *Phys Rev B Condens Matter Mater Phys* **2014**, *89*, DOI 10.1103/PhysRevB.89.174102.
[20] M. Tanaka, *Acta Crystallographica Section A* **1994**, *50*, 261.
[21] M. Y. Gureev, A. K. Tagantsev, N. Setter, *Phys Rev B Condens Matter Mater Phys* **2011**, *83*, DOI 10.1103/PhysRevB.83.184104.
[22] J. Zhang, Y. J. Wang, J. Liu, J. Xu, D. Wang, L. Wang, X. L. Ma, C. L. Jia, L. Bellaiche, *Phys Rev B* **2020**, *101*, DOI 10.1103/PhysRevB.101.060103.
[23] J. Sapriel, *Phys Rev B* **1975**, *12*, 5128.
[24] F. Xue, Y. Gu, L. Liang, Y. Wang, L. Q. Chen, *Phys Rev B Condens Matter Mater Phys* **2014**, *90*, DOI 10.1103/PhysRevB.90.220101.
[25] R. Beanland, *Acta Crystallographica Section A* **2011**, *67*, 191.
[26] J. Seidel, L. W. Martin, Q. He, Q. Zhan, Y. H. Chu, A. Rother, M. E. Hawkridge, P. Maksymovych, P. Yu, M. Gajek, N. Balke, S. v. Kalinin, S. Gemming, F. Wang, G. Catalan, J. F. Scott, N. A. Spaldin, J. Orenstein, R. Ramesh, *Nat Mater* **2009**, *8*, 229.
[27] C. T. Nelson, B. Winchester, Y. Zhang, S. J. Kim, A. Melville, C. Adamo, C. M. Folkman, S. H. Baek, C. B. Eom, D. G. Schlom, L. Q. Chen, X. Pan, *Nano Lett* **2011**, *11*, 828.
[28] C. M. Folkman, S. H. Baek, H. W. Jang, C. B. Eom, C. T. Nelson, X. Q. Pan, Y. L. Li, L. Q. Chen, A. Kumar, V. Gopalan, S. K. Streiffer, *Appl Phys Lett* **2009**, *94*, DOI 10.1063/1.3152009.
[29] L. Li, P. Gao, C. T. Nelson, J. R. Jokisaari, Y. Zhang, S. J. Kim, A. Melville, C. Adamo, D. G. Schlom, X. Pan, *Nano Lett* **2013**, *13*, 5218.
[30] Y. Qi, Z. Chen, C. Huang, L. Wang, X. Han, J. Wang, P. Yang, T. Sritharan, L. Chen, in *J Appl Phys*, **2012**.
[31] W. Y. Wang, Y. L. Tang, Y. L. Zhu, Y. bin Xu, Y. Liu, Y. J. Wang, S. Jagadeesh, X. L. Ma, *Adv Mater Interfaces* **2015**, *2*, DOI 10.1002/admi.201500024.
[32] L. Li, J. Britson, J. R. Jokisaari, Y. Zhang, C. Adamo, A. Melville, D. G. Schlom, L. Q. Chen, X. Pan, *Advanced Materials* **2016**, *28*, 6574.
[33] P. S. Bednyakov, B. I. Sturman, T. Sluka, A. K. Tagantsev, P. v. Yudin, *NPJ Comput Mater* **2018**, *4*, DOI 10.1038/s41524-018-0121-8.
[34] C. T. Nelson, B. Winchester, Y. Zhang, S. J. Kim, A. Melville, C. Adamo, C. M. Folkman, S. H. Baek, C. B. Eom, D. G. Schlom, L. Q. Chen, X. Pan, *Nano Lett* **2011**, *11*, 828.
[35] L. Li, Y. Zhang, L. Xie, J. R. Jokisaari, C. Beekman, J. C. Yang, Y. H. Chu, H. M. Christen, X. Pan, *Nano Lett* **2017**, *17*, 3556.
[36] L. Li, X. Cheng, J. R. Jokisaari, P. Gao, J. Britson, C. Adamo, C. Heikes, D. G. Schlom, L. Q. Chen, X. Pan, *Phys Rev Lett* **2018**, *120*, DOI 10.1103/PhysRevLett.120.137602.

[37] L. Li, X. Cheng, T. Blum, H. Huyan, Y. Zhang, C. Heikes, X. Yan, C. Gadre, T. Aoki, M. Xu, L. Xie, Z. Hong, C. Adamo, D. G. Schlom, L. Q. Chen, X. Pan, *Nano Lett* **2019**, *19*, 6812.
[38] H. Yang, J. G. Lozano, T. J. Pennycook, L. Jones, P. B. Hirsch, P. D. Nellist, *Nat Commun* **2015**, *6*, DOI 10.1038/ncomms8266.
[39] A. Lubk, S. Gemming, N. A. Spaldin, *Phys Rev B Condens Matter Mater Phys* **2009**, *80*, DOI 10.1103/PhysRevB.80.104110.
[40] Y. Wang, C. Nelson, A. Melville, B. Winchester, S. Shang, Z. K. Liu, D. G. Schlom, X. Pan, L. Q. Chen, *Phys Rev Lett* **2013**, *110*, DOI 10.1103/PhysRevLett.110.267601.
[41] C. L. Jia, V. Nagarajan, J. Q. He, L. Houben, T. Zhao, R. Ramesh, K. Urban, R. Waser, *Nat Mater* **2007**, *6*, 64.
[42] P. Paruch, J. Guyonnet, *C R Phys* **2013**, *14*, 667.
[43] L. Liu, K. Xu, Q. Li, Y. Huang, L. Shu, Y. Y. S. Cheng, S. Zhang, J. Luo, J. Zhu, J. F. Li, *Adv Funct Mater* **2022**, DOI 10.1002/adfm.202207730.
[44] D. Lee, R. K. Behera, P. Wu, H. Xu, S. B. Sinnott, S. R. Phillpot, L. Q. Chen, V. Gopalan, *Phys Rev B Condens Matter Mater Phys* **2009**, *80*, DOI 10.1103/PhysRevB.80.060102.
[45] J. Y. Chauleau, T. Chirac, S. Fusil, V. Garcia, W. Akhtar, J. Tranchida, P. Thibaudeau, I. Gross, C. Blouzon, A. Finco, M. Bibes, B. Dkhil, D. D. Khalyavin, P. Manuel, V. Jacques, N. Jaouen, M. Viret, *Nat Mater* **2020**, *19*, 386.
[46] H. Gao, C. Chen, L. You, F. Sun, C. Lu, S. Yang, G. Zhou, D. Chen, Y. Han, J. M. Liu, *Adv Opt Mater* **2022**, *10*, DOI 10.1002/adom.202200831.

The table of contents entry should be 50–60 words long and should be written in the present tense. The text should be different from the abstract text.

Wanbing Ge*, Richard Beanland, Marin Alexe, and Ana M. Sanchez*

3D Reconstruction of Sawtooth 180° Tail-to-Tail Domain Walls in Single Crystal $BiFeO_3$

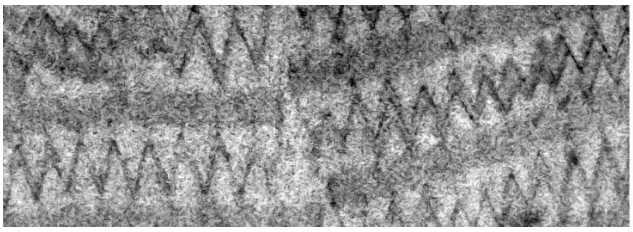

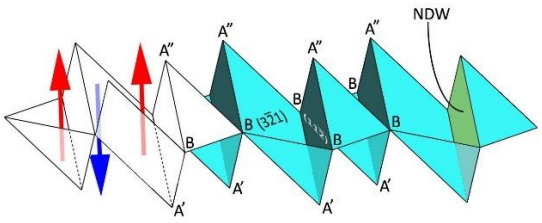

We re-examine the dense structure of alternating sawtooth and flat ferroelectric domain walls found in high quality single crystal $BiFeO_3$. Using electron diffraction, TEM and aberration-corrected STEM we show that all domain walls are of 180° type, and propose a 3D model of this complex microstructure. The tail-to-tail sawtooth structure minimises the local charge density of the domain wall.

Supporting Information

3D Reconstruction of Sawtooth 180° Tail-to-Tail Domain Walls in Single Crystal $BiFeO_3$

Wanbing Ge, Richard Beanland, Marin Alexe and Ana M. Sanchez*

1. Piezo-response force microscopy

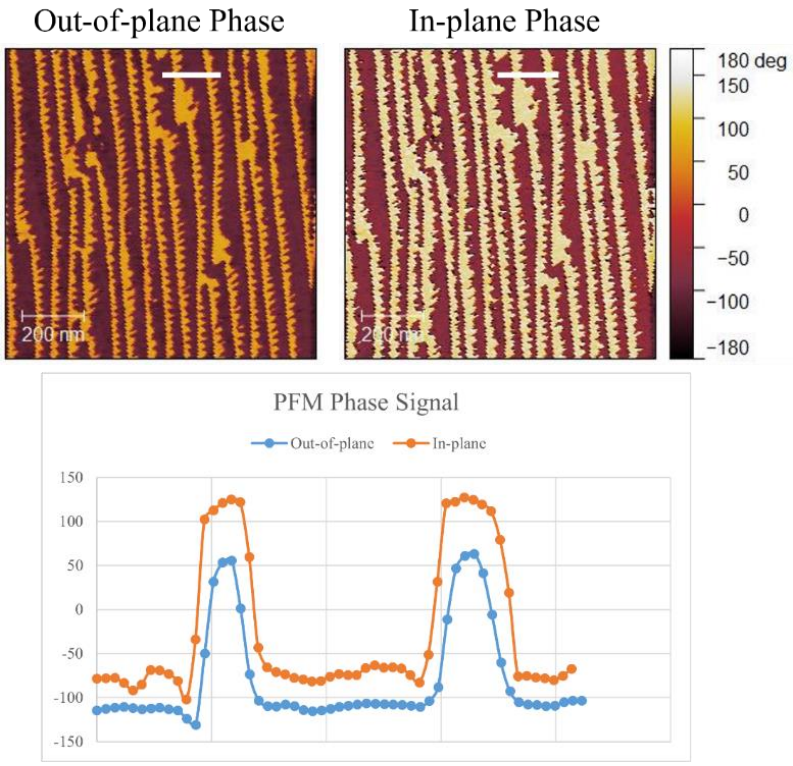

Figure S1. (Top) A typical set of simultaneously collected PFM out-of-plane and in-plane phase signals (scan direction horizontal) on a polished (001) $BiFeO_3$ surface, showing a 180° phase change at both sawtooth and flat domain walls. (Bottom) Plots of the PFM phase along the white lines marked on the PFM images.

2. Neutral domain wall facets

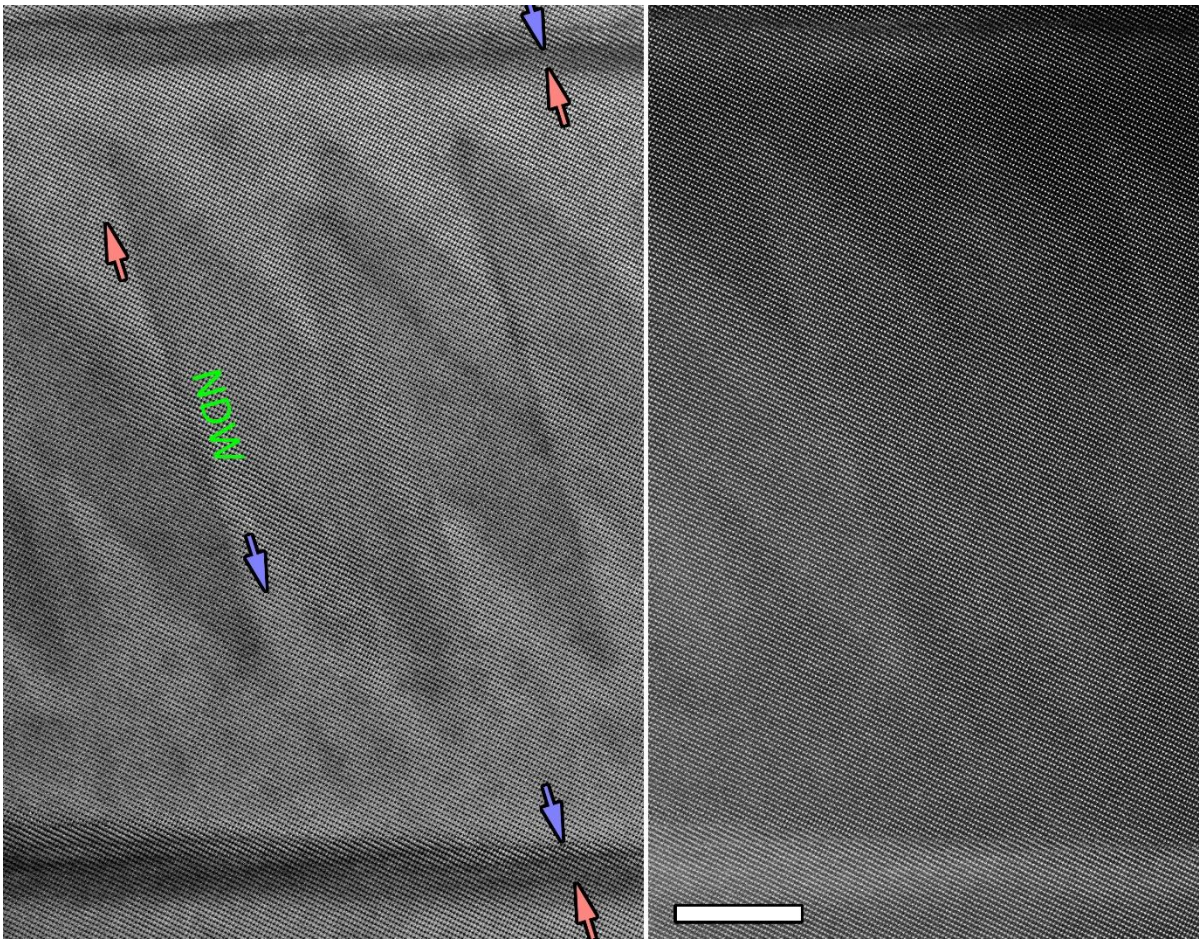

Figure S2. Sawtooth DW structure when seen from $[\bar{1}10]$ Bright field STEM (left) and annular dark field STEM (right), scale bar 10 nm. Polarisation directions are indicated and a $(11\bar{2})$ NDW facet labelled.